Radiation dose and image quality in K-edge subtraction computed tomography of lung *in vivo*

S. Strengell,[a,b]* J. Keyriläinen,[b] P. Suortti,[a] S. Bayat,[c] A. R. A. Sovijärvi[d] and L. Porra[a]

[a]Department of Physics, University of Helsinki, Helsinki 00370, Finland, [b]Department of Oncology, Helsinki University Central Hospital, Helsinki, Finland, [c]Université de Picardie Jules Verne, Inserm U1105 and CHU Amiens, France, and [d]Department of Clinical Physiology and Nuclear Medicine, Helsinki University Central Hospital, Helsinki, Finland. *E-mail: satu.strengell@helsinki.fi

K-edge subtraction computed tomography (KES-CT) allows simultaneous imaging of both structural features and regional distribution of contrast elements inside an organ. Using this technique, regional lung ventilation and blood volume distributions can be measured experimentally *in vivo*. In order for this imaging technology to be applicable in humans, it is crucial to minimize exposure to ionizing radiation with little compromise in image quality. The goal of this study was to assess the changes in signal-to-noise ratio (SNR) of KES-CT lung images as a function of radiation dose. The experiments were performed in anesthetized and ventilated rabbits using inhaled xenon gas in O_2 at two concentrations: 20% and 70%. Radiation dose, defined as air kerma (K_a), was measured free-in-air and in a 16 cm polymethyl methacrylate phantom with a cylindrical ionization chamber. The dose free-in-air was varied from 2.7 mGy to 8.0 Gy. SNR in the images of xenon in air spaces was above the Rose criterion (SNR > 5) when K_a was over 400 mGy with 20% xenon, and over 40 mGy with 70% xenon. Although in human thorax attenuation is higher, based on these findings it is estimated that, by optimizing the imaging sequence and reconstruction algorithms, the radiation dose could be further reduced to clinically acceptable levels.

Keywords: dosimetry; computed tomography; K-edge subtraction; image quality; lung imaging.

1. Introduction

K-edge subtraction (KES) computed tomography (CT) imaging uses synchrotron radiation (SR) to quantify the distribution of contrast elements with high Z. Typically used biocompatible contrast agents are iodine, xenon and gadolinium, for which K-edges range from 33 to 51 keV. Two CT images are acquired simultaneously using X-ray energies that bracket the absorption edge of the contrast agent. The difference between the images provides the distribution of the contrast agent in absolute units. An advantage of this technique is that both structural images and elemental distribution maps, which allow functional parameters to be measured, can be obtained simultaneously using the same imaging modality. The KES-CT imaging technique has previously been used to measure regional lung ventilation during stable xenon gas inhalation (Bayat *et al.*, 2001, 2006, 2009; Porra *et al.*, 2004, 2010; Strengell *et al.*, 2013), and to measure regional blood volume distribution during steady-state iodine infusion (Suhonen *et al.*, 2008) in rabbit. This technique is promising for the early diagnosis of focal changes in regional lung function,

at early stages of diseases such as asthma, chronic obstructive pulmonary disease (COPD) or cystic fibrosis, that routine measurements of global lung function and gas exchange are unable to detect.

High spatial resolution in morphological assessment of ventilation and direct quantification are the advantages of the KES method in comparison with MRI with hyperpolarized He(3) gas, SPECT (single-photon emission computed tomography) and PET (positron emission tomography). KES is a special case of dual-energy CT (DECT), which is already available for clinical practice. However, KES avoids several limitations of DECT, where continuous spectra from a dual-source X-ray tube are used. Each material has a specific attenuation curve, which allows separation of different tissues or contrast agents with the same density (Avrin *et al.*, 1978). In DECT, the materials with similar attenuation curves cannot be distinguished (Fornaro *et al.*, 2011) and also the ventilation images with contrast agent are still not directly quantified (Chae *et al.*, 2008; Honda *et al.*, 2012). The energy spectrum of X-rays from conventional X-ray sources is wide and non-monochromatic, which causes artefacts in the images and

increases the error of concentration measurements. For clinical applications this excludes the comparison of the images taken in different imaging times, *i.e.* in the follow-up of asthmatic or COPD patients.

The KES imaging method has previously been applied for human coronary angiography using injected iodine as contrast agent (Rubenstein *et al.*, 1986), and several studies were performed with clinically acceptable radiation doses (Suortti *et al.*, 1993; Dix, 1995; Elleaume *et al.*, 2000; Dix *et al.*, 2003; Suortti & Thomlinson, 2003;

Figure 1
Schematic view of the synchrotron *K*-edge imaging set-up in dose measurements.

Bertrand *et al.*, 2005). Sensitivity of the KES imaging technique and the relationship between the image quality and radiation dose has been studied earlier theoretically and with phantoms using variable concentrations of iodine and gadolinium as contrast agents (Sarnelli *et al.*, 2006). The feasibility of imaging airways with Xe has previously been demonstrated in a human subject (Giacomini *et al.*, 1998).

However, the feasibility of KES-CT imaging of regional lung structure and function in humans critically depends on exposure to ionizing radiation. Although there is a substantial margin for the reduction of radiation exposure in this imaging modality, reducing radiation dose can potentially affect image quality. Technically the lower limit of radiation exposure is set by the inherent detector noise and the upper limit by the detector saturation. Within these limits, the minimum exposure is determined by the requirements of image quality and contrast intensity, and the maximum exposure by the acceptable radiation dose. However, the optimal compromise between ionizing radiation exposure and the quality of *in vivo* Xe KES-CT images has not been assessed before.

The goal of the present study was to assess the relation between dose and image quality in *in vivo* lung KES-CT imaging of inhaled Xe gas distribution within the lung. This relation is crucial for determining whether this imaging technique can be performed with clinically acceptable radiation doses in human subjects.

2. Materials and methods

2.1. *K*-edge subtraction imaging

The KES-CT imaging technique uses dual SR beams at two slightly different energies below and above the *K*-edge of a contrast element, such as inhaled stable Xe gas in the air spaces (Porra *et al.*, 2004; Monfraix *et al.*, 2005) or infused iodine contrast in blood (Suhonen *et al.*, 2008) (Fig. 1). Based on these two simultaneously recorded CT images, the distribution of the contrast element within the imaged organ can be measured. The difference between the images is based on the property that the attenuation coefficient of the contrast element suddenly increases when the energy of the incident X-ray beam rises above the *K*-energy threshold. For example,
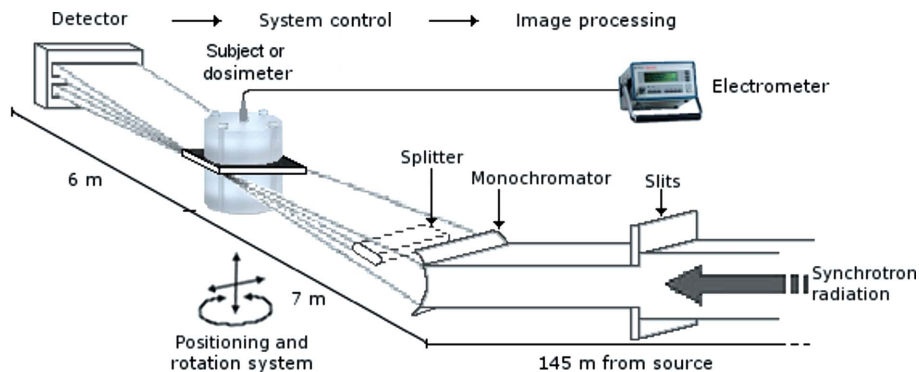
the attenuation coefficient of Xe increases over five-fold when the energy of the incident beam exceeds 34.56 keV (Bayat *et al.*, 2001). Subtraction of the two images reveals a quantitative image of contrast agent inside the organ. Using the dual-energy KES-CT imaging method, the absolute density due to tissue or to the contrast agent can be calculated separately. The two acquired images are subtracted before the reconstruction, and tissue and Xe density images are reconstructed separately using a computer algorithm explained in detail elsewhere (Sarnelli *et al.*, 2005). The concentration of the contrast agent can be measured within each voxel or region of interest from the Xe density images. Functional parameters such as regional gas volume and ventilation are calculated from the Xe density images (Porra *et al.*, 2004; Monfraix *et al.*, 2005). Anatomical details, such as central airway dimensions and parenchymal density, can be assessed from the tissue density images, which resemble conventional CT images (Bayat *et al.*, 2013). This imaging technique requires a SR source, since as opposed to standard X-ray sources it allows the selection of monochromatic beams from the wide X-ray spectrum while conserving enough intensity for imaging and decreasing dose.

2.1.1. Experimental set-up. All measurements were performed at the Biomedical beamline (ID17) of the European Synchrotron Radiation Facility (ESRF, Grenoble, France). The instrumentation of ID17 has been described in detail elsewhere (Elleaume *et al.*, 1999). In a typical KES-CT imaging arrangement, two mono-energetic beams are produced from the continuous SR spectrum by a cylindrically bent silicon crystal monochromator (Suortti *et al.*, 2000). A wiggler SR source with 20 full-field poles was used. The characteristic (median) energy of the continuous spectrum was 17.36 keV at a wiggler gap of 55 mm. The radiation fan was limited at the beamline entrance by a diaphragm to 1 mrad (horizontal) and 0.067 mrad (vertical). Soft X-rays were removed by graphite and aluminium filters. A slit in front of the monochromator limited the vertical height of the beam to 6.00 mm, and a tantalum beam-splitter blocked 2.7 mm at the centre of the beam. The vertical position of the splitter defines the difference of the intensities of two beams. The horizontal and vertical profiles of the two monochromatic beams are shown in Fig. 2. The energies E_{Low} and E_{High} are

determined by scanning the monochromator and recording the intensity behind a Xe-gas absorber (Suortti *et al.*, 1993). At the Xe *K*-edge (34.56 keV) the slit and the splitter pass about 24% of the total vertical distribution. The bent crystal trans-
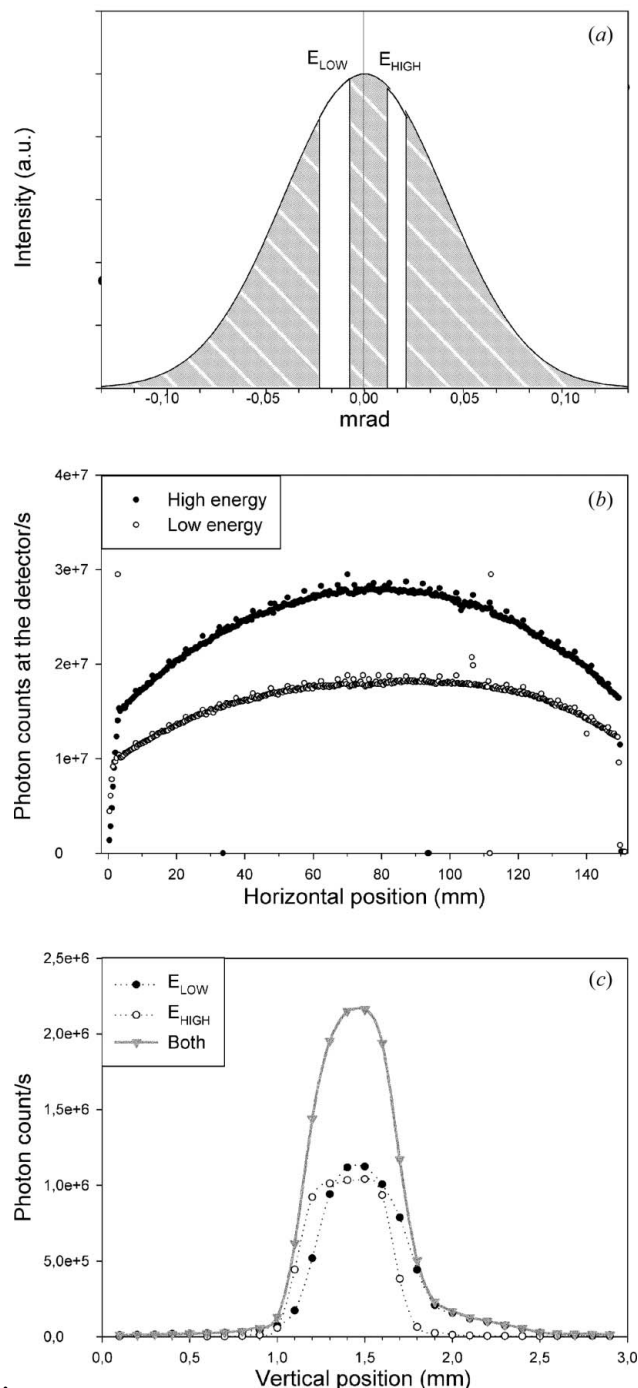
mission (Laue-type) monochromator reflects two beams, below (E_{Low}) and above (E_{High}) the Xe *K*-edge energy (E_K), each with an energy span of 170 eV, separated by 250 eV (centre-to-centre). The beam energies bracketed the Xe *K*-edge: $E_{Low} < E_K < E_{High}$, and the beams were focused to fans, which overlapped at the focus point, 7 m downstream. The source-to-monochromator distance is 145 m, monochromator-to-subject distance is 7 m, and subject-to-detector distance is 6 m.

The beam height was determined by scanning a narrow slit across the beam at the focus. The average height at the centre of the beam was 0.63 ± 0.07 mm. Bending and asymmetric cutting of the monochromator crystal increases the integrated reflectivity by an order of magnitude as compared with that of a flat perfect crystal (Erola *et al.*, 1990; Suortti *et al.*, 1993). The beam intensity at the focus is almost 100 times larger than the intensity from a flat perfect crystal monochromator without focusing.

2.1.2. Data acquisition. A liquid-nitrogen-cooled (77 K) germanium detector (EGPS, Eurisys Mesures, Lingolsheim, France) was used. The detector consists of a 160 mm-long monolithic germanium crystal, which is segmented into two rows of 432 parallel strips with a pitch of 0.35 mm. The two rows, 0.5 mm apart, allow simultaneous recording of each of the two beams. The 2.5 mm-thick germanium crystal with 0.5 mm-thick beryllium windows provides a high X-ray absorption efficiency of nearly 100% at 20 keV and 88% at 60 keV. The modulation transfer function shows the first zero values at 2.9 and 5.7 line-pairs mm^{-1}, and, at the 10% level, 2.5, 3.2 and 5.0 line-pairs mm^{-1} (Bravin *et al.*, 2003). The 16-bit dynamic range of the electronics allows signals to be recorded over more than four decades. The system has excellent linearity and low noise level, down to about 5 pA (Elleaume *et al.*, 1999).

The dose measurements were performed during a typical *in vivo* animal experiment using the usual imaging set-up (Porra *et al.*, 2004). This allows for unbiased comparison of the image quality and radiation dose. The exposure time, determined by the beam shutter, was measured by the integration time of the beam-monitoring ionization chambers at the entrance of the imaging hutch. The exposure time interval of 3.76 s included a ramp-up of the CT rotation motor acceleration, a 360° rotation in 2 s, followed by a ramp-down.

Because of the static SR beam geometry, the imaged object is rotated about the axis perpendicular to the beams (6.56° off-vertical) for CT imaging and moved vertically for projection imaging. In the horizontal direction, spatial resolution is determined by the 0.35 mm spacing of the strips (pixel size). In the vertical direction, spatial resolution in CT imaging is determined by the height of the beam. The rotation speed in CT imaging was 180° s^{-1} and projections were recorded at 0.5° intervals (720 projections per CT slice). Reconstruction of the CT images was performed using a conventional filtered backprojection algorithm (FBP) (Bracewell & Riddle, 1967), which was applied to the use of KES-CT imaging (Sarnelli *et al.*, 2005) using Interactive Data Language (IDL; RSI, Boulogne-Billancourt, France).

Figure 2
Vertical and horizontal profiles of the beam. (*a*) Schematic figure of the vertical profile of the dual beam passed by the 6.0 mm slit and the splitter. (*b*) Vertical scans of the beams at the focus. 'Low energy' indicates the beam energy below the *K*-edge of xenon and 'High energy' the beam above the *K*-edge of xenon, and 'Both' indicates the sum of the beams. (*c*) Horizontal profiles of the beams at the Ge detector. The difference in intensity is due to a small off-centring of the beam splitter. The image intensities are brought to the same scale and flat-field by using these white-field intensities.

research papers

2.2. Radiation dose

Radiation dose was determined in three different ways: (i) based on the radiation source parameters and beamline optics; (ii) using the signal intensity recorded by the germanium detector, and (iii) measured free-in-air and in a phantom with a cylindrical ionization chamber.

2.2.1. Estimated dose based on the source. The absorbed dose is defined as the imparted energy dE per unit mass element dm (Graeff & Engelke, 1991):

$$D = \frac{dE}{dm} = \Phi_0 E_{ph} \left(\frac{\mu}{\rho}\right)_{en}, \qquad (1)$$

where $\Phi_0 = N_0/A$ is the photon flux on area A, E_{ph} is the photon energy, and $(\mu/\rho)_{en}$ is the mass energy absorption coefficient. This involves the assumption that no energy escapes the volume of interest as high-energy electrons or X-ray bremsstrahlung. This is the case at low photon energies (about 35 keV in the present measurement); therefore, D equals the air kerma (K_a; kinetic energy released per unit mass). The power of the monochromatic beams, defined by the energy of the beam divided by exposure time, and D can be calculated with fair accuracy from the properties of the SR source and the X-ray optics of the beamline.

The dose rate at the focus, where the object is placed, is calculated from the intensity of the two X-ray beams. The absorbed power per unit volume is

$$\frac{dP}{dV} = I\mu_{en} = \left(\frac{P}{hw}\right)\mu_{en} = \left(\frac{P_0}{hw}\right)\mu_{en} \cot\theta \int R(\theta)\, d\theta, \qquad (2)$$

where I is the intensity of the incident beam, P_0 the incident power, μ_{en} the energy absorption coefficient, h and w the height and width of the focused beam, respectively, θ the Bragg angle and $R(\theta)$ the reflectivity of the monochromator crystal (Erola *et al.*, 1990; Suortti *et al.*, 1993).

2.2.2. Estimated dose based on the detector. The Ge detector allows absolute measurement of the beam intensity (Elleaume *et al.*, 2002). The photon flux N_0 incident on a detector pixel is obtained from the cumulated charge, which is digitized multiplying by the number of electron–hole pairs created by a photon and dividing by the minimum detectable charge. The energy of the elementary beam is $N_0 E_{ph}$, and it is converted to absorbed dose at the focus, where the beam height is measured (Table 1). The photon flux, as the number of photons N_0 incident on the detector per pixel, is calculated as (Elleaume *et al.*, 2002)

$$N_0 = \exp(\mu_{Be} x_{Be}) N Q_{min} E_p$$
$$\times \frac{128}{E_{ph}[1 - \exp(-\mu_{Ge} x_{Ge})]\, \bar{e} \times \text{gain}}, \qquad (3)$$

where the first term corresponds to the detector entrance beryllium window transmission factor: μ_{Be} is the attenuation coefficient of beryllium, x_{Be} the thickness of the beryllium window, N the detector reading (bits) in one pixel, Q_{min} the minimum detectable charge (2×10^{-15} C), E_p the mean

Table 1
Measured and calculated photon flux and absorbed dose rate at the imaging position without plexiglass attenuators in the SR beam.

The Ge detector readings were corrected for air absorption and surrounding temperature and pressure, and scaled to correspond to a ring electron current of 80 mA.

	Dosimeter	Detector	Theoretical
P_{KL} rate (mGy s^{-1} cm)	134.31 ± 0.40		
Photon flux ($\times 10^{12}$ photons s^{-1} cm^{-2})	3.73 ± 0.41	3.77 ± 0.42	3.41 ± 0.38
Dose rate (Gy s^{-1})	2.13 ± 0.24	2.16 ± 0.24	1.95 ± 0.22

energy necessary to create an electron–hole pair in germanium (2.98 eV), E_{ph} the photon energy of the monochromatic beam (34.56 keV), μ_{Ge} the total attenuation coefficient of germanium (cm^{-1}), x_{Ge} the detector thickness (0.25 cm), $\bar{e}$ the electron charge (1.602×10^{-19} C) and 'gain' is the electronic gain of the detector (1 in the present case). For beryllium and germanium, attenuation coefficients are interpolated and calculated from tabulated data (NIST, 2014).

The photon fluence φ_0 is

$$\varphi_0 = \frac{\Phi_0}{dt} = \frac{N_0}{wh\, dt}, \qquad (4)$$

where w is the pixel width of the detector (0.35 mm), h is the beam height (0.63 mm) and dt is the integration time of one projection at the detector (2.22 ms).

When calculating the dose at the sample position at 6 m distance from the detector, the difference of the pixel width at the sample position and attenuation of the air between the sample and detector were taken into account. The absorbed dose was calculated using equation (1).

2.2.3. Dosimetry. The experiments were designed to relate the radiation dose measurement in KES-CT imaging to dosimetry in clinical practice using standard protocols in medical X-ray imaging (ICRU, 2005; IAEA, 2007). A pencil-shaped ionization chamber was used for its reliability (uncertainty below 5%), re-usability and conformity with internationally accepted procedures (Oliviera *et al.*, 2011). The dosimeter integrates K_a and yields the air kerma length product (P_{KL}) in mGy cm,

$$P_{KL} = \int_L K_a(L)\, dL = K_a L, \qquad (5)$$

where L is the integral height of the beam. P_{KL} was measured free-in-air and divided by the beam height to yield K_a in mGy at the beam focus and divided by exposure time to yield the dose rate in mGy s^{-1}. P_{KL} was measured also in a standard tissue-equivalent 16 cm-diameter polymethyl methacrylate (PMMA, $\rho = 1.19$ g cm^{-3}) cylinder head phantom in order to determine the computed tomography air kerma index ($C_{K,PMMA}$). A 15 cm-long pencil-shaped ionization chamber [type 77336; Physikalisch-Technische Werkstätten (PTW), Freiburg, Germany] was used, and the ionization chamber was connected to an electrometer (Unidos; PTW, Freiburg, Germany).

Each dose value was obtained from the mean value of the electrometer readings for three separate scans normalized to a synchrotron storage ring current of 80 mA and corrected for temperature and pressure. For studies of system linearity and possible effects of beam hardening, the incident photon flux was varied by inserting plexiglass attenuators into the monochromatic beams. The thickness of the attenuators varied from 0 to 26 cm, resulting in a photon flux reduction by four orders of magnitude. There is no trace of beam hardening or nonlinear response of the dosimeter as the logarithm of intensity falls off linearly with the attenuator thickness (Fig. 3). The attenuation coefficient agrees closely with the tabulated value (NIST, 2014).

The CT air kerma index, $C_{K,PMMA}$, referred to in practice as the computed tomography dose index (CTDI or CD) (Leitz *et al.*, 1995), was derived from P_{KL} in a single rotation for slice thickness L (ICRU, 2005),

$$C_{K,PMMA} = (1/L) \int_{-\infty}^{\infty} K_{a,PMMA}(z)\,dz = P_{KL,PMMA}/L. \quad (6)$$

For proper averaging, the ion chamber was placed sequentially at the centre (c) and four holes in the periphery (p) of the phantom (3, 6, 9 and 12 o'clock positions). The weighted average of the centre and peripheral dose index was defined as (Leitz *et al.*, 1995)

$$C_{K,PMMA,w} = \frac{C_{K,PMMA,c} + 2C_{K,PMMA,p}}{3}. \quad (7)$$

Commercial CT scanners provide a volume-based index $C_{K,PMMA,vol}$, which depends on the choice of imaging parameters and takes exposure variation along the z axis, perpendicular to the beam plane, into account, but is independent of the scan length. In the present case where the phantom is not scanned axially, $C_{K,PMMA,vol}$ is the same as $C_{K,PMMA,w}$. $C_{K,PMMA,w}$ was calculated from P_{KL} values for a standard cylinder head phantom. The head phantom was chosen because of the limited width of the beam in the current set-up.
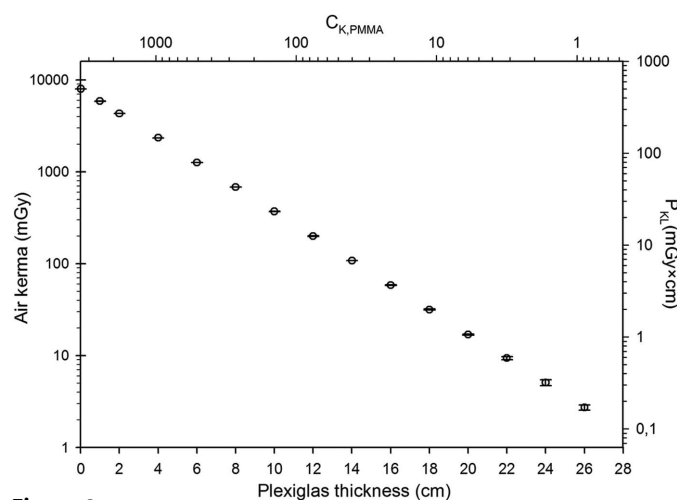

Figure 3
Computed tomography index ($C_{K,PMMA,w}$) for the 16 cm head PMMA phantom, air kerma (K_a) and air kerma length product (P_{KL}) as functions of the plexiglass attenuator thickness, 0 to 26 cm.

2.3. Animal experiments

2.3.1. Animal preparation. Animal care and experimental procedures were in accordance with the Guide for the Care and Use of Laboratory Animals (ILAR, 2011) and approved by the local institutional authorities. Experiments were performed in two mechanically ventilated New Zealand male rabbits (2.70 and 2.85 kg; Elevage Scientifique des Dombes, Chatillon sur Chalaronne, France). Animals were anesthetized by Midazolam (0.2 mg kg^{-1} h^{-1} IV; Aguettant, Lyon, France), paralyzed by IV Atracurium (1.0 mg kg^{-1} h^{-1}; Tracrium, GlaxoSmithKline, Münchenbuchsee, Switzerland), and tracheostomized with an endotracheal tube (No. 3; Portex, Berck sur Mer, France). The animal was immobilized in the vertical position in a plastic holder, which leaves the diaphragm and chest free. Blood pressure, endotracheal pressure and respiratory flow were continuously monitored throughout the experiment.

2.3.2. Imaging protocol and image analysis. Tissue-density and Xe-density CT images were used to evaluate the image quality as a function of air kerma K_a, measured free-in-air. The signal-to-noise ratio (SNR) was calculated from various regions in the images as the incident beam was attenuated by 0–26 cm of plexiglass (*cf.* Fig. 3). Two different inhaled gas mixtures were used, $(20 \pm 6)\%$ Xe + air for rabbit A and $(70 \pm 14)\%$ Xe + O_2 for rabbit B, measured from the main bronchus of the rabbit. The duration of a ventilation cycle was 1.2 s (inspiration 0.5 s and expiration 0.7 s) and the images were acquired after 21 respiratory cycles so that the stable values of the Xe density were reached in the airspaces. Ventilation was paused at end-expiration during image acquisition for 3 s, and the images were recorded during the apnea. The signal (S) in the reconstructed CT images was determined within five regions-of-interest selected inside the lumen of five main bronchi, in spinal muscle, in the lung parenchyma, and within large blood vessels and heart chambers. The background signal was measured outside the animal or phantom and its standard deviation SD$_{bg}$ was calculated. SNR was defined as

$$\mathrm{SNR} = S/\mathrm{SD}_{bg}. \quad (8)$$

Images were processed using the Matlab (MathWorks Inc., Natick, MA, USA) programming package and calculations of image quality were performed with *ImageJ* software (National Institutes of Health, USA).

2.4. Statistical analysis

Dose parameters, K_a, P_{KL}, $C_{K,PMMA,w}$, beam height and dose rate are expressed as mean $\pm$ SD. For estimating the precision of the image quality measurements, SNR is expressed as mean $\pm$ standard error of the mean.

3. Results

3.1. Dose measurements

Results of dose measurements and calculations are given in Table 1. The variability of dosimeter readings was tested by comparing five separate measurements. The standard devia-

tion from the mean value was less than 0.3%. There was a close agreement between the dose rates measured by the pencil dosimeter and the Ge detector with the value calculated from the source parameters and beamline optics. $C_{K,PMMA,w}$ as a function of P_{KL} is shown in Fig. 3. The perfect linear dependence of $C_{K,PMMA,w}$ on K_a demonstrates the absence of beam hardening in the plexiglass. On the other hand, it can be seen that $C_{K,PMMA}$ is about 30% of K_a, although a ten-fold reduction would be expected at the centre of the phantom due to beam attenuation. The large value of $C_{K,PMMA}$ arises from multiple Compton scattering in the phantom, so that the dosimeter is imbedded in a diffuse radiation source.

3.2. Radiation dose and image quality

CT images of rabbit lungs are shown in Fig. 4 at different dose levels, regulated by plexiglass attenuators with thicknesses varying from zero to 26 cm. The upper rows of Fig. 4 show the tissue density images, which are due to beam attenuation in the various tissue structures. The lower rows show the distribution of Xe gas in the airways and alveoli.

The SNR values of the images are shown in Figs. 5 and 6. In the tissue density images, SNR of the Xe phantom and the bronchial lumen remained below the detection limit SNR = 5 (Rose, 1973), as expected. The mass attenuation coefficients of muscle and lung tissue were almost equal, so that it is seen in Fig. 5 that the density of muscle is higher than the density of

lung tissue due to the presence of air. The signal from lung tissue remained above the detection limit when the integrated dose (air kerma during the scan) was larger than 3 mGy.

In the Xe density image (rabbit A, Fig. 6a), the signal from the dorsal muscle was zero, indicating a complete removal of the tissue signal by the image-subtraction algorithm. In the bronchial lumen, SNR stayed above the detection limit when the integrated dose was larger than 60 mGy at 20% Xe concentration (see Fig. 6a). In the lung parenchyma, the detection limit was reached at approximately 400 mGy (see Fig. 6a). When the Xe concentration was increased to 70% (rabbit B, Fig. 6b), the threshold values for Xe in the main bronchial lumen and lung air spaces were about 40 mGy.

4. Discussion

The goal of this study was to assess the relation between radiation dose and image quality in *in vivo* KES-CT imaging of inhaled Xe gas distribution within the lung. Our results show that: (i) KES imaging allows measuring the distribution of 20% Xe gas distribution; (ii) KES-CT of inhaled Xe using a synchrotron source can be performed with clinically acceptable radiation doses. This finding is significant, since several ongoing projects aim at developing compact synchrotron X-ray light sources, which have the potential to make this technology available in the clinical setting in the future (Schlenvoigt *et al.*, 2008; Schleede *et al.*, 2012; Meinel *et al.*,
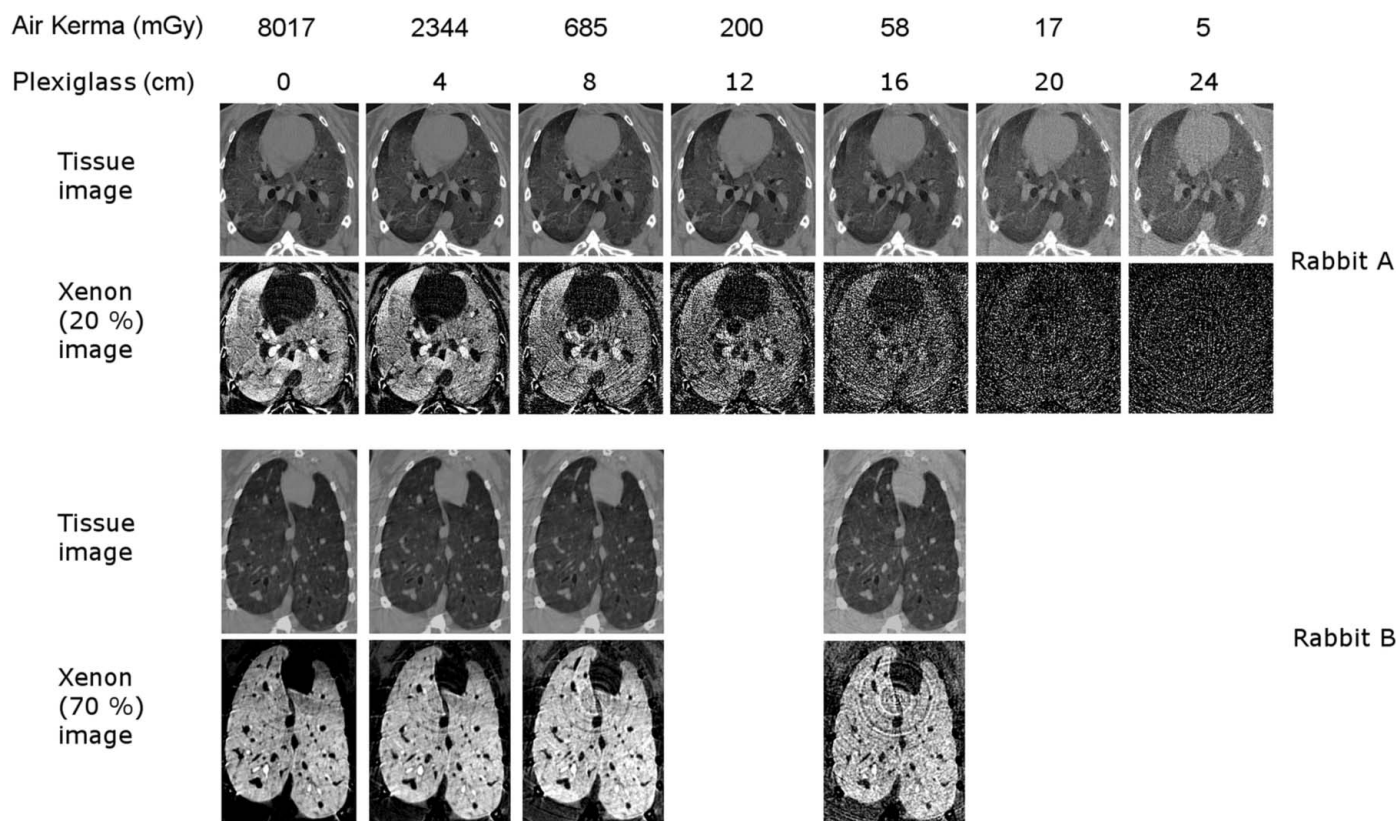

Figure 4
Tissue density and xenon density images of rabbit lung for different air kerma doses and plexiglass thicknesses with two xenon concentrations of the inhaled gas: 20% (rabbit *A*, upper rows) and 70% (rabbit *B*, lower rows).

2013), although improvements in the energy range and radiation flux of such sources limit their applicability at the moment. In the meantime, low-dose KES-CT can be useful for high-throughput longitudinal functional imaging of small animals.

We assessed the quality of lung KES-CT images during Xe inhalation, as a function of radiation dose. In the Xe density images the detection limit was exceeded with a radiation dose of 60 mGy with a 20% inhaled Xe concentration (Fig. 6a). A lower radiation dose value of 40 mGy was measured with a 70% Xe concentration (Fig. 6b).

The recommended clinical dose for a high-resolution chest CT is currently 35 mGy ($C_{K,PMMA,w}$) using a 32 cm PMMA phantom without any contrast agent (EC, 2000). This value corresponds to 71 mGy using a 16 cm PMMA phantom (AAPM, 2011). With the present imaging set-up, the detection limit (SNR = 5) of Xe within the lung airspaces was reached at a $C_{K,PMMA,w}$ of 14 mGy (70% Xe) and 21 mGy (20% Xe) as shown in Fig. 6. The comparison between the measured and recommended dose values suggests that SR KES-CT imaging with pitch of 1 (couch travel/slice thickness) would be feasible with clinically acceptable doses.

The advantage of KES-CT for imaging the distribution of an inert gas in the lung is that both the lung structure and the gas distribution can be separately but simultaneously imaged. As seen in the tissue density CT image (Fig. 5), the SNR of Xe in the airway lumen does not rise above the detection limit. However, in the Xe density images, only Xe gas is detected and the rest of the tissue is subtracted away (Fig. 6).

A limitation of this imaging technique in human subjects is that inhalation of 28–35% end-tidal xenon concentrations can cause sedation (Bedi et al., 2002, 2003) and a 70% Xe concentration is commonly used in human anesthesia (Lugunbühl et al., 2005; Lachmann et al., 1990). In this study we found that low Xe gas concentrations of 20% within the airways and lung parenchyma could be imaged with a radiation dose of 60 mGy ($C_{K,PMMA,w}$ = 21 mGy). This is a substantial improvement as compared with CT with standard X-ray sources, where Xe concentrations as low as 20% are not or are barely detectable (Chon et al., 2007). In the present study the contrast enhancement measured during 20% Xe inhalation was 110 HU. This value is over twice as much as previously measured using 30% Xe with a standard CT machine, which was less than 50 HU (Chon et al., 2007). As expected, the radiation dose required to fulfil the image quality criterion of SNR = 5 decreased at higher Xe concentrations of 70%. Although Xe gas has anesthetic properties at such concentrations, the volume of inhaled gas can be limited to a single tidal volume or even less in human subjects (Xu et al., 2012), thereby limiting sedative side-effects.

There is a wide margin to reduce radiation dose exposure in SR KES-CT imaging. Using an optimal exposure time of 2 s, the detection limit of the bronchial lumen could be reached at $C_{K,PMMA,w}$ = 7 mGy and that of the lung parenchyma at $C_{K,PMMA,w}$ = 11 mGy, without a compromise in the image quality. In the present experiments, the applied exposure time of 3.75 s included ramp-up and ramp-down of the CT rotation motor acceleration, before and after image acquisition. This
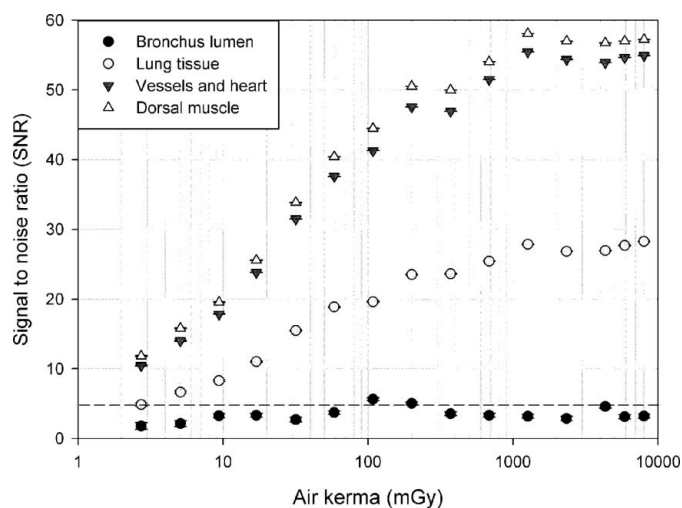

Figure 5
Signal-to-noise ratio (SNR) as a function of air kerma (K_a) in different parts of a tissue density image of rabbit A. The dashed line demonstrates the detection limit of SNR = 5 (Rose criterion).
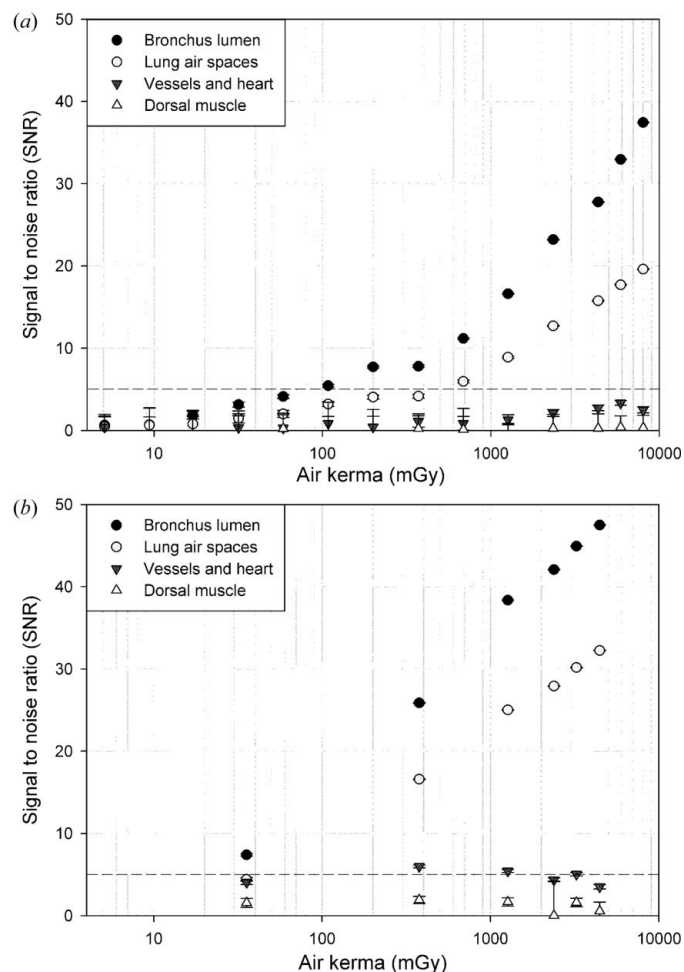
Figure 6
Signal-to-noise ratio (SNR) as a function of air kerma (K_a) calculated from KES-CT images of rabbit lung with (a) 20% (rabbit A) and (b) 70% (rabbit B) of xenon in inhaled gas. The dashed line demonstrates the detection limit of SNR = 5 (Rose criterion).

exposure time can be can be reduced to exclude acceleration times in the future.

We previously measured the quantitative distribution of regional lung ventilation by sequential KES-CT imaging during Xe wash-in or wash-out (Porra *et al.*, 2004). Repeating KES image acquisitions multiplies the radiation dose exposure. However, we have previously demonstrated that essential information on the regional distribution of lung ventilation can be derived from single subtraction images (Porra *et al.*, 2009). Also the exposure reduction may be gained by reducing the CT image acquisition to 180° instead of 360°. However, an effect of the reduction in the number of angular projections on image quality cannot be excluded. The replacement of analytic image reconstruction methods (*e.g.* FBP) by more versatile but computationally more expensive iterative reconstruction methods may reduce the required number of projections, and thus the radiation dose. The ongoing advances in computer speed and memory have assisted in the utilization of more and more effective (faster) iterative algorithms, and dose reductions of 50% to 65% have been reported in chest imaging (Hou *et al.*, 2012; Yamada *et al.*, 2012; Kalra *et al.*, 2013; Mueck *et al.*, 2013). It has been demonstrated that in SR phase-contrast CT imaging of a breast tumor the number of projections may be reduced by a factor of four when the equally sloped tomography (EST) algorithm is used (Zhao *et al.*, 2012). In preliminary data we found that interpretable Xe-density images can be obtained with 72 projections and a multiplicative algebraic reconstruction (MAR) algorithm. Furthermore, reducing projections by gating the image acquisition with a synchronized shutter action (Renier *et al.*, 2005) can further decrease the exposure time and doses are reduced by a factor of ten.

We found that dose measurements with a pencil dosimeter are in good agreement with the absolute flux measurements with the Ge detector, and this is confirmed by calculation from the source parameters and beamline optics. The response of the dosimeter to the incident X-ray flux varied within four decades, from P_{KL} = 505 mGy cm (dose rate = 2.1 Gy s^{-1}) to P_{KL} = 0.17 mGy cm (dose rate = 0.7 mGy s^{-1}). The acceptable radiation doses in animal studies and in human imaging with SR are well within these limits, so that reliable dosimetry may be performed on-line with a pencil dosimeter.

5. Conclusions

Synchrotron KES-CT imaging of inhaled Xe gas distribution in the lung is a unique method for *in vivo* assessment of regional lung ventilation and structure with a high spatial resolution. The present study demonstrates that limitations due to radiation exposure can be overcome while maintaining sufficient contrast resolution for quantitative mapping of ventilation. Our findings suggest that KES-CT is applicable as a valuable investigative modality for imaging regional function in human lungs. Further study is needed in order to develop a dedicated imaging set-up and to validate appropriate imaging protocols.

References

AAPM (2011). *AAPM Report No. 204*. American Association of Physicists in Medicine, College Park, MD 20740, USA.

Avrin, D. E., Macovski, A. & Zatz, L. E. (1978). *Invest. Radiol.* **13**, 217–222.

Bayat, S., Le Duc, G., Porra, L., Berruyer, G., Nemoz, C., Monfraix, S., Fiedler, S., Thomlinson, W., Suortti, P., Standertskjöld-Nordenstam, C. G. & Sovijärvi, A. R. A. (2001). *Phys. Med. Biol.* **46**, 3287–3299.

Bayat, S., Porra, L., Albu, G., Suhonen, H., Strengell, S., Suortti, P., Sovijärvi, A. R. A., Peták, F. & Habre, W. (2013). *Anesthesiology*, **119**, 89–100.

Bayat, S., Porra, L., Suhonen, H., Nemoz, C., Suortti, P. & Sovijärvi, A. R. A. (2006). *J. Appl. Physiol.* **100**, 1964–1973.

Bayat, S., Strengell, S., Porra, L., Janosi, T. Z., Petak, F., Suhonen, H., Suortti, P., Hantos, Z., Sovijärvi, A. R. A. & Habre, W. (2009). *Am. J. Respir. Crit. Care Med.* **180**, 296–303.

Bedi, A., McCarroll, C., Murray, J. M., Stevenson, M. A. & Fee, J. P. (2002). *Anaesthesia*, **57**, 233–241.

Bedi, A., Murray, J. M., Dingley, J., Stevenson, M. A. & Fee, J. P. (2003). *Crit. Care Med.* **31**, 2470–2477.

Bertrand, B., Estève, F., Elleaume, H., Nemoz, C., Fiedler, S., Bravin, A., Berruyer, G., Brochard, T., Renier, M., Machecourt, J., Thomlinson, W. & Le Bas, J. F. (2005). *Eur. Heart J.* **26**, 1284–1291.

Bracewell, R. N. & Riddle, A. C. (1967). *Astrophys. J.* **150**, 427.

Bravin, A., Fiedler, S., Coan, P., Labiche, J.-C., Ponchut, C., Peterzol, A. & Thomlinson, W. (2003). *Nucl. Instrum. Methods Phys. Res. A*, **510**, 35–40.

Chae, E. J., Seo, J. B., Goo, H. W., Kim, N., Song, K. S., Lee, S. D., Hong, S. J. & Krauss, B. (2008). *Radiology*, **248**, 615–624.

Chon, D., Beck, K. C., Simon, B. A., Shikata, H., Saba, O. I. & Hoffman, E. A. (2007). *J. Appl. Physiol.* **102**, 1535–1544.

Dix, W. R. (1995). *Prog. Biophys. Mol. Biol.* **63**, 159–191.

Dix, W.-R., Kupper, W., Dill, T., Hamm, C. W., Job, H., Lohmann, M., Reime, B. & Ventura, R. (2003). *J. Synchrotron Rad.* **10**, 219–227.

EC (2000). *European Commission Report Eur 16262 EN*. Luxembourg: Office for Official Publication of the European Communities.

Elleaume, H., Charvet, A. M., Berkvens, P., Berruyer, G., Brochard, T., Dabin, Y., Dominguez, M. C., Draperi, A., Fiedler, S., Goujon, G., Le Duc, G., Mattenet, M., Nemoz, C., Perez, M., Renier, M., Schulze, C., Spanne, P., Suortti, P., Thomlinson, W., Esteve, F., Bertrand, B. & Le Bas, J. F. (1999). *Nucl. Instrum. Methods Phys. Res. A*, **428**, 513–527.

Elleaume, H., Charvet, A. M., Corde, S., Estève, F. & Le Bas, J. F. (2002). *Phys. Med. Biol.* **47**, 3369–3385.

Elleaume, H., Fiedler, S., Esteve, F., Bertrand, B. & Charvet, A. M. (2000). *Phys. Med. Biol.* **45**, 39–43.

Erola, E., Eteläniemi, V., Suortti, P., Pattison, P. & Thomlinson, W. (1990). *J. Appl. Cryst.* **23**, 35–42.

Fornaro, J., Leschka, S., Hibbeln, D., Butler, A., Anderson, N., Pache, G., Scheffel, H., Wildermuth, S., Alkadhi, H. & Stolzmann, P. (2011). *Insights Imaging*, **2**, 149–159.

Giacomini, J. C., Gordon, H., O'Neil, R., Van Kessel, A., Cason, B., Chapman, D., Lavendar, W., Gmur, N., Menk, R., Thomlinson, W., Zhong, Z. & Rubenstein, E. (1998). *Nucl. Instrum. Methods Phys. Res. A*, **406**, 473–478.

Graeff, W. & Engelke, K. (1991). *Handbook on Synchrotron Radiation*, Vol. 4, edited by S. Ebashi, M. Koch and E. Rubenstein, pp. 361–405. Amsterdam: Elsevier.

Honda, N., Osada, H., Watanabe, W., Nakayama, M., Nishimura, K., Krauss, B. & Otani, K. (2012). *Radiology*, **262**, 262–268.

Hou, Y., Xu, S., Guo, W., Vembar, M. & Guo, Q. (2012). *Eur. J. Radiol.* **81**, 3905–3911.

IAEA (2007). *Technical Report Series No. 457*. Vienna: International Atomic Energy Agency.

ICRU (2005). *ICRU Report 74*. Bethesda: International Commission on Radiation Units and Measurements.

ILAR (2011). *Guide for the Care and Use of Laboratory Animals*. Institute for Laboratory Animal Research. Washington: National Academies Press.

Kalra, M. K., Woisetschläger, M., Dahlström, N., Singh, S., Digumarthy, S., Do, S., Pien, H., Quick, P., Schmidt, B., Sedlmair, M., Shepard, J. O. & Persson, A. (2013). *Am. J. Roentgenol.* **201**, W235–W244.

Lachmann, B., Armbruster, S., Schairer, W., Landstra, M., Trouwborst, A., Van Daal, G. J., Kusuma, A. & Erdmann, W. (1990). *Lancet*, **335**, 1413–1415.

Leitz, W., Axelsson, B. & Szendro, G. (1995). *Radiat. Prot. Dosim.* **57**, 377–380.

Lugunbühl, M., Petersen-Felix, S., Zbinden, A. M. & Schnider, T. W. (2005). *Can J. Anaesth.* **52**, 38–44.

Meinel, F. G., Schwab, F., Schleede, S., Bech, M., Herzen, J., Achterhold, K., Auweter, S., Bamberg, F., Yildirim, A. Ö, Bohla, A., Eickelberg, O., Loewen, R., Gifford, M., Ruth, R., Reiser, M. F., Pfeiffer, F. & Nikolaou, K. (2013). *PLoS One*, **8**, e59526.

Monfraix, S., Bayat, S., Porra, L., Berruyer, G., Nemoz, C., Thomlinson, W., Suortti, P. & Sovijärvi, A. R. A. (2005). *Phys. Med. Biol.* **50**, 1–11.

Mueck, F. G., Michael, L., Deak, Z., Scherr, M. K., Maxien, D., Geyer, L. L., Reiser, M. & Wirth, S. (2013). *Rofo*, **185**, 644–654.

NIST (2014). *Physical Reference Data*, Gaithersburg, MD: National Institute of Standards and Technology (http://physics.nist.gov/PhysRefData/).

Oliveira, B., Mourão, A. & da Silva, T. (2011). *World Acad. Sci. Eng. Technol.* **80**, 88–91.

Porra, L., Bayat, S., Strengell, S., Suhonen, H., Sovijärvi, A. R. A. & Suortti, P. (2009). *American Thoracic Society International Conference* 15–20 May 2009, San Diego, USA. Presentation A1061.

Porra, L., Monfraix, S., Berruyer, G., Le Duc, G., Nemoz, C., Thomlinson, W., Suortti, P., Sovijärvi, A. R. A. & Bayat, S. (2004). *J. Appl. Physiol.* **96**, 1899–1908.

Porra, L., Peták, F., Strengell, S., Neitola, K., Janosi, T. Z., Suhonen, H., Suortti, P., Sovijärvi, A. R. A., Habre, W. & Bayat, S. (2010). *Am. J. Physiol. Lung Cell. Mol. Physiol.* **299**, L242–L251.

Renier, M., Fiedler, S., Nemoz, C., Gonzalez, H., Berruyer, G. & Bravin, A. (2005). *Nucl. Instrum. Methods Phys. Res. A*, **548**, 111–115.

Rose, A. (1973). *Vision: Human and Electronic*. New York: Plenum.

Rubenstein, E., Hofstadter, R., Zeman, H. D., Thompson, A. C., Otis, J. N., Brown, G. S., Giacomini, J. C., Gordon, H. J., Kernoff, R. S., Harrison, D. C. & Thomlinson, W. (1986). *Proc. Natl Acad. Sci. USA*, **83**, 9724–9728.

Sarnelli, A., Elleaume, H., Taibi, A., Gambaccini, M. & Bravin, A. (2006). *Phys. Med. Biol.* **51**, 4311–4328.

Sarnelli, A., Nemoz, C., Elleaume, H., Estève, F., Bertrand, B. & Bravin, A. (2005). *Phys. Med. Biol.* **50**, 725–740.

Schleede, S., Meinel, F. G., Bech, M., Herzen, J., Achterhold, K., Potdevin, G., Malecki, A., Adam-Neumair, S., Thieme, S. F., Bamberg, F., Nikolaou, K., Bohla, A., Yildirim, A. Ö, Loewen, R., Gifford, M., Ruth, R., Eickelberg, O., Reiser, M. & Pfeiffer, F. (2012). *Proc. Natl Acad. Sci. USA*, **109**, 17880–17885.

Schlenvoigt, H.-P., Haupt, K., Debus, A., Budde, F., Jäckel, O., Pfotenhauer, S., Schwoerer, H., Rohwer, E., Gallacher, J. G., Brunetti, E., Shanks, R. P., Wiggins, S. M. & Jaroszynski, D. A. (2008). *Nat. Phys.* **4**, 130–133.

Strengell, S., Porra, L., Sovijärvi, A. R. A., Suhonen, H., Suortti, P. & Bayat, S. (2013). *Respir. Physiol. Neurobiol.* **189**, 465–472.

Suhonen, H., Porra, L., Bayat, S., Sovijärvi, A. R. A. & Suortti, P. (2008). *Phys. Med. Biol.* **53**, 775–791.

Suortti, P., Fiedler, S., Bravin, A., Brochard, T., Mattenet, M., Renier, M., Spanne, P., Thomlinson, W., Charvet, A. M., Elleaume, H., Schulze-Briese, C. & Thompson, A. C. (2000). *J. Synchrotron Rad.* **7**, 340–347.

Suortti, P. & Thomlinson, W. (2003). *Phys. Med. Biol.* **48**, R1–R35.

Suortti, P., Thomlinson, W., Chapman, D., Gmür, N., Siddons, D. P. & Schulze, C. (1993). *Nucl. Instrum. Methods Phys. Res. A*, **336**, 304–309.

Xu, X., Norquay, G., Parnell, S. R., Deppe, M. H., Ajraoui, S., Hashoian, R., Marshall, H., Griffiths, P. D., Parra-Robles, J. & Wild, J. M. (2012). *Magn. Reson. Med.* **68**, 1900–1904.

Yamada, Y., Jinzaki, M., Hosokawa, T., Tanami, Y., Sugiura, H., Abe, T. & Kuribayashi, S. (2012). *Eur. J. Radiol.* **81**, 4185–4195.

Zhao, Y., Brun, E., Coan, P., Huang, Z., Sztrókay, A., Diemoz, P. C., Liebhardt, S., Mittone, A., Gasilov, S., Miao, J. & Bravin, A. (2012). *Proc. Natl Acad. Sci. USA*, **109**, 18290–18294.